PAPER

Check for updates

Light-driven methane conversion: unveiling methanol using a TiO₂/TiOF₂ photocatalyst†

Wibawa Hendra Saputera, [ID] *[abc] Gita Yuniar[a] and Dwiwahju Sasongko[ac]

A TiO₂/TiOF₂ composite has been synthesized through a hydrothermal method and characterized using X-ray diffraction, Raman spectroscopy, UV-vis diffuse reflectance, SEM-EDX, TEM, and N₂ adsorption–desorption isotherms. The percentage of exposed facet [001] and the composition of TiO₂/TiOF₂ in the composite were controlled by adjusting the amount of HF and hydrothermal temperature synthesis. Three crucial factors in the photocatalytic conversion of methane to methanol, including the photocatalyst, electron scavenger (FeCl₂), and H₂O₂ were evaluated using a statistical approach. All factors were found to have a significant impact on the photocatalytic reaction and exhibited a synergistic effect that enhanced methanol production. The highest methanol yield achieved was $0.7257\ \mu\text{mole h}^{-1}\ \text{g}_{cat}^{-1}$. The presence of exposed [001] and fluorine (F) in the catalyst is believed to enhance the adsorption of reactant molecules and provide a more oxidative site. The Fenton cycle reaction between FeCl₂ and H₂O₂ was attributed to reducing recombination and extending the charge carrier lifetime. Incorporating Ag into the TiO₂/TiOF₂ catalyst results in a significant 2.2-fold enhancement in methanol yield. Additionally, the crucial involvement of hydroxyl radicals in the comprehensive reaction mechanism highlights their importance in influencing the process of photocatalytic methane-to-methanol conversion.

Introduction

Methane (CH₄), the simplest hydrocarbon, has garnered growing interest as a potential alternative energy source. It is widely recognized as a greenhouse gas with a greater global warming potential than carbon dioxide (CO₂). However, it possesses the highest hydrogen-to-carbon (H/C) ratio among all hydrocarbons and boasts a substantial calorific value, making it a promising energy resource. Methane has a symmetric tetrahedral structure and exhibits low polarizability, as well as low electron and proton affinity.[1] The conversion of methane is a challenging process from a kinetic standpoint due to its stability and non-reactive nature. To initiate the reaction, substantial energy supply in the form of high pressure and temperature is required.

Utilizing methane gas directly as an energy source presents challenges in terms of handling, storage, and transportation. Therefore, it is more advantageous to obtain a liquid product from methane conversion. Methanol has emerged as the

favored product of methane conversion because it retains the high calorific value of methane and can be directly employed as a fuel source.

The most commonly used method for converting methane into methanol at present is steam reforming, but this approach is associated with significant energy consumption and expense. Recent technological efforts have concentrated on devising a method to convert methane into methanol under ambient conditions. Photocatalytic technology has garnered considerable interest in the realm of renewable energy because it provides an efficient means to produce methanol using solar energy, which is a renewable resource, without the need for extreme operating conditions.

Until now, numerous research studies have been conducted to identify the optimal photocatalyst for facilitating the photocatalytic conversion of methane into methanol. Researchers have explored various semiconductors for this purpose, including TiO₂, WO₃, ZnO, NiO, and Fe₂O₃. A modification also applied to semiconductors, such as the incorporation of RuO_x onto ZnO/CeO₂, enhances the photocatalytic efficiency in producing methanol from methane and water. This enhancement results from an improved separation of interfacial charge and an elevation of free hydroxyl radical species.[2]

The ideal semiconductor photocatalyst should possess specific characteristics: it must be chemically and biologically inert, maintain photocatalytic stability, be easy to produce and utilize, be activatable with low-energy light such as sunlight, be

[a]Department of Chemical Engineering, Research Group on Sustainable Energy and Technology, Faculty of Industrial Technology, Institut Teknologi Bandung, Jl. Ganesha no. 10, Bandung 40132, Indonesia. E-mail: whsaputera@itb.ac.id

[b]Center for Catalysis and Reaction Engineering, Institut Teknologi Bandung, Jl. Ganesha no. 10, Bandung 40132, Indonesia

[c]Research Center for New and Renewable Energy, Institut Teknologi Bandung, Jl. Ganesha no. 10, Bandung 40132, Indonesia

† Electronic supplementary information (ESI) available. See DOI: https://doi.org/10.1039/d4ra00353e

cost-effective, and be environmentally friendly.[3] Titanium dioxide (TiO_2) stands out as the most widely utilized semiconductor for photocatalysis due to its wide bandgap, affordability, high photocatalytic activity, robust photostability, nontoxic nature, abundant availability, insolubility in aqueous solutions, and chemical and biological inertness.[4]

Pure titanium dioxide possesses a wide bandgap that obstructs its ability to harness direct sunlight effectively.[5] Various modifications have been implemented on the semiconductor to overcome this limitation, including the creation of heterojunctions,[6] doping,[7] rearranging crystal facets,[8] altering its structure and electronic properties.[9]

Recent advancements and strategies in photocatalytic of methane to methanol conversion have been comprehensively reported covering aspects such as materials design comprises heterojunction, cocatalyst decoration, and assistance with oxidants, along with engineering prospects.[10,11] Doping is a commonly employed modification strategy to optimize the properties of photocatalysts. In elemental doping, impurities, whether metals or non-metals doping, are intentionally introduced into an intrinsic semiconductor. Exploration of doping have been reported with metals such as Au,[12] metal-doped,[13] and self-doping.[14] Additionally, chemical agents are introduced into the system to enhance the overall process through the generation of OH$^\cdot$ from H_2O_2 and serve as electron scavengers to capture electrons, thereby preventing the recombination of charge carriers (electrons and holes) and simultaneously improving methanol yield.[15]

Currently, there is a growing interest in modifying TiO_2-based catalysts by incorporating $TiOF_2$. This composite material has found widespread application in photocatalytic reactions, including the degradation of ammonia,[8] hydrogen evolution,[16] degradation of pollutant.[17] The $TiO_2/TiOF_2$ composite can be easily synthesized through a one-step hydrothermal process, utilizing titanium butoxide and hydrogen fluoride as precursors.[18,19] This modification encourages crystal growth in the desired [001] facet direction. Moreover, additional substances such as H_2O_2 and electron scavengers are introduced into the system to prevent electron–hole recombination and thus improve the yield and selectivity towards the desired products. However, it's worth noting that some research papers have reported varying findings on this matter.

To date, there has been no documentation of the utilization of the $TiO_2/TiOF_2$ composite in the photocatalytic conversion of methane to methanol. This study aims to explore the impact of supplementary substances like H_2O_2 and electron scavengers using a statistical approach. The research will delve into the photocatalytic conversion process of methane to methanol,

taking into account three critical factors: the photocatalyst, H_2O_2, and an electron scavenger.

Experimental section

Materials

Titanium butoxide ($Ti(OBu)_4$), hydrogen fluoride (HF), hydrogen peroxide (H_2O_2), and iron(II) chloride ($FeCl_2$) were procured from Sigma Aldrich. Additionally, commercial titanium dioxide P25, which served as a reference photocatalyst, was also obtained from Sigma Aldrich. Methane and argon gases were sourced from CV Sangkuriang in Indonesia.

Sample preparation

The TiO_2 photocatalysts were prepared using a method outlined in the existing literature, with certain adjustments incorporated for modification.[20] Variations in the photocatalysts were achieved by altering the quantities of HF and the reaction temperature, and the specific conditions are elaborated upon in Table 1.

Briefly, $Ti(OBu)_4$ reagent was introduced into a Teflon autoclave with a capacity of 20 mL. Subsequently, a gradual addition of HF solution into the autoclave took place, followed by thorough mixing through vortexing. The resulting mixture underwent a hydrothermal reaction under specified conditions. Afterward, the system was allowed to naturally cool down to room temperature, and the precipitate was separated from the liquid *via* centrifugation, followed by a thorough wash with ethanol. The sample was then subjected to drying in an oven at 60 °C for a duration of 3 hours and subsequently placed in a desiccator to eliminate any remaining moisture. Finally, the dried solid was ground to obtain the white catalyst powder.

The Ag-loaded $TiO_2/TiOF_2$ catalyst was prepared by *in situ* photodeposited reactions of $AgNO_3$ with $TiO_2/TiOF_2$ sample. Briefly, 0.1 g of the prepared $TiO_2/TiOF_2$ was suspended in an anaerobic aqueous solution containing 20 mL of deionized water, 5 mL of CH_3OH, and 1 wt% of $AgNO_3$. After 30 min irradiation under 300 W Xe lamp, the products were collected *via* centrifugation, washed with water and dried at 60 °C.

Characterizations

The catalysts crystal structures were analyzed under ambient conditions using X-ray diffraction (XRD, Bruker D8 Advance, Billerica, Massachusetts, USA). Cu-Kα radiation with a wavelength (λ) of 0.15406 nm was employed for this purpose. To estimate the crystallite size, the Scherrer equation was applied, utilizing the full width at half the maximum height of the peak observed at $2\theta = 28.9°$. Diffuse reflectance spectra were obtained *via* a UV-Vis spectrophotometer (Thermo Scientific Evolution 200,

Table 1 Photocatalyst synthesis details

Reagent	Hydrothermal reaction condition	Catalyst code
5 mL Ti(Obu)$_4$ + 0.4 mL HF	180 °C, 24 hours	Ti-A
5 mL Ti(Obu)$_4$ + 0.8 mL HF	200 °C, 24 hours	Ti-B

Waltham, Massachusetts, USA) and converted into absorbance values using the Kubelka–Munk method, with $BaSO_4$ serving as the reference material. To examine the morphology of the catalyst, a scanning electron microscope (SEM, SU3500, Hitachi High-Technologies Corporation, Tokyo, Japan) and transmission electron microscopy (TEM, H9500, Hitachi High-Technologies Corporation, Tokyo, Japan) were used. Nitrogen physisorption measurements were conducted at a temperature of 77 K using a specific surface area analyzer (Quantachrome Nova 4200e Instruments, USA). Before the adsorption measurements, the samples underwent degassing at 150 °C for 3 hours. Specific surface areas were calculated using the Brunauer–Emmett–Teller (BET) method, and porosity parameters were determined using the Barrett–Joyner–Halenda (BJH) method. Raman spectra were recorded with a Raman spectrometer (Bruker-Senterra, Billerica, Massachusetts, USA) equipped with a 514 nm argon-ion laser. The production of hydroxyl radical ($^\bullet$OH) by the UV-illuminated $TiO_2/TiOF_2$ catalysts was assessed using a photoluminescence (PL) method with coumarin as the probe molecule. Coumarin readily reacts with $^\bullet$OH to produce a highly fluorescent product, 7-hydroxycoumarin (7HC). The experimental procedure was similar to the photocatalytic activity measurements, except that water was replaced by a coumarin aqueous solution (5×10^{-4} M). Samples were collected at 30 minute intervals and filtered through a membrane filter. The PL spectra of the generated 7HC were monitored at $\lambda_{max} = 454$ nm when excited at $\lambda_{exc} = 332$ nm. Fluorescence spectra were measured using a spectrofluorometer (Hitachi F-2700).

Photocatalytic tests

The evaluation of the photocatalytic performance of the synthesized $TiO_2/TiOF_2$ catalyst for methane-to-methanol conversion was conducted within a specially configured batch photoreactor. This reactor is equipped with a 300 W xenon lamp emitting UV-visible light and a cooling system to maintain the ambient temperature. The photocatalyst was dissolved in distilled water to achieve a concentration of 1 g L^{-1}. This mixture was then introduced into the reactor, with a magnetic stirrer facilitating mass transfer between the photocatalyst and the reactants. Before initiating the reaction, the reactor was purged with argon gas, followed by the introduction of methane gas into the mixture, which continued for 15 minutes. The reaction was initiated by turning on the light source. Samples were extracted from both the liquid and gas phases at 30 minute intervals for analysis using Gas Chromatography (Shimadzu 14B, Japan). The gas phase was analyzed to determine methane conversion, while the liquid phase was analyzed to calculate methanol yield.

Statistical analysis

The experiment was devised using a statistical approach, employing a two-level full factorial design of experiment. The factors and their respective levels utilized in this two-level full-factorial experimental design are detailed in Table 2.

The experimental design layout was generated by Minitab software program. For this experiment, a single replicate was

Table 2 Factors and corresponding levels in the experimental design

Factors	−1 (low level)	+1 (high level)
Photocatalyst	Ti-A	Ti-B
Electron scavenger ($FeCl_2$)	0	15 mL
H_2O_2	0	1 mL

Table 3 Experiment design parameters and conditions

Std order	Run order	Center Pt	Blocks	Catalyst	$FeCl_2$	H_2O_2
5	R1	1	1	Ti-A	0.0	1.0
1	R2	1	1	Ti-A	0.0	0.0
6	R3	1	1	Ti-B	0.0	1.0
10	R4	0	1	Ti-B	7.5	0.5
7	R5	1	1	Ti-A	15.0	1.0
4	R6	1	1	Ti-B	15.0	0.0
3	R7	1	1	Ti-A	15.0	0.0
2	R8	1	1	Ti-B	0.0	0.0
8	R9	1	1	Ti-B	15.0	1.0
9	R10	0	1	Ti-A	7.5	0.5

conducted with eight experimental runs (2^3 run order) and two additional centre points were included. Consequently, the experimental design layout comprised a total of 10 runs as outlined in Table 3.

ANOVA (Analysis of Variance) was employed to identify the influential factors, including the specific levels that yield the most pronounced signals arising from both the primary factors and their interactions. In this experiment, a 95% confidence interval was utilized. Consequently, parameters with p-values below 0.05 were deemed to exert a statistically significant influence on the experimental response. To assess the suitability of the model, a residual analysis was conducted. This examination of residuals allows for the detection of various types of model inadequacies and violations of the underlying assumptions.

Result and discussion

Analysis of characterization results

X-ray diffraction (XRD). Fig. 1 clearly shows the crystal structure of prepared samples. Both samples exhibit a similar diffraction pattern, characterized by a prominent peak at 28° (ref. 21) corresponding to anatase TiO_2 and a strong diffraction peak at 23.39° attribute to $TiOF_2$.[22] These observed peaks align with the standard spectrum of TiO_2 (JCPDS no. 21-1272; $2\theta = 25.28, 36.94, 37.80, 38.57, 48.04, 53.89, 55.06, 62.68, 70.31°$) and $TiOF_2$ (JCPDS no. 01-0490; $2\theta = 13.61, 23.39, 27.68, 33.41, 47.83, 53.89, 59.59, 69.58,$ and $74.68°$).

Ti-B showed exhibited a notably stronger peak in the (100) crystal plane of $TiOF_2$ suggesting a higher content $TiOF_2$ within the composite. The composition of each element, TiO_2 and $TiOF_2$, was further confirmed through the reference intensity ratio, resulting in a $TiO_2 : TiOF_2$ ratio of 88 : 12 for Ti-A and 45 : 55 for Ti-B.
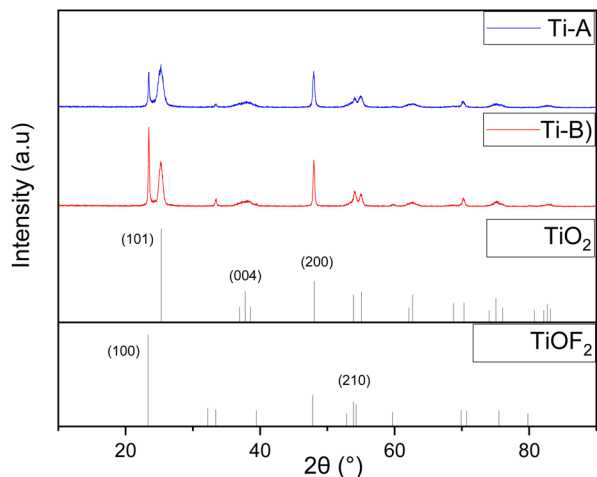
Paper

Fig. 1 XRD patterns of the prepared samples.

Fig. 2 UV-vis absorption of the prepared samples.

The presence of Ti^{4+} from $TiOBu_4$ and F^- from HF plays a pivotal role in the synthesis of $TiO_2/TiOF_2$ composites, as highlighted in a study by Li *et al.*[17] Notably, the characteristics of the $TiOF_2$ peaks became more distinct with increased HF content during the synthesis reaction, indicating the higher proportion of $TiOF_2$ within the heterojunction.[17] Furthermore, F^- ions in HF contribute to the stabilization of the [001] crystal orientation, thereby influencing crystal formation, as previously observed by Han *et al.* and Ong *et al.*[20,23] This influence is discernible in the diffraction patterns of Ti-A and Ti-B, where the intensity and sharpness of the (200) peak surpass that of the (004) peak, indicating a preference for crystal growth along the [001] plane.[24]

UV-vis diffuse reflectance spectroscopy (UV-vis DRS). UV-vis diffuse reflectance spectroscopy analysis was conducted to assess the optical characteristics of the synthesized catalyst. The introduction of TiO_2 and $TiOF_2$ heterojunctions was undertaken with the aim of mitigating the issue of visible light scattering, a limitation associated with pure TiO_2. Both catalysts display a comparable peak in the 200–400 nm range, signifying their equivalent capacity to absorb UV light. Ti-A exhibited a greater redshift capability compared to Ti-B, suggesting that Ti-A possesses better visible light absorption characteristics (Fig. 2 and 3).

The bandgap values serve as indicators of a photocatalyst's light absorption capability. In terms of electronic band structures, both TiO_2 and $TiOF_2$ share similar characteristics, wherein the valence band is primarily composed of 2p O and/or F orbitals, while the conduction band is primarily comprised of 3d Ti orbitals.[5] Introducing the appropriate quantity of HF during the synthesis of $TiO_2/TiOF_2$ has the potential to enhance visible light absorption.[25] The formation of a $TiO_2/TiOF_2$ heterojunction involves the insertion of F^- ions into the O^{2-} sites on TiO_2, requiring an additional electron to balance the charge. This process reduces Ti^{4+} to Ti^{3+}. The self-doping of Ti^{3+} can increase the conductivity of TiO_2 and enhance the separation and movement of electron–hole charge pairs.[26] Additionally, Ti^{3+} defects from Ti–O bond synthesized *via* flame spray pyrolysis were able to facilitate the oxidation and reduction processes of water into hydrogen and oxygen.[27]
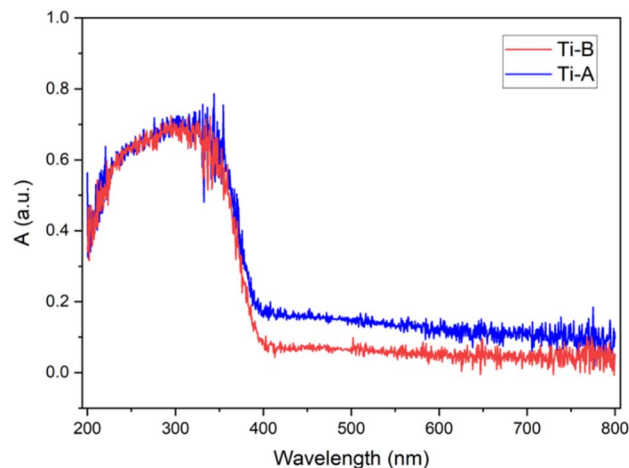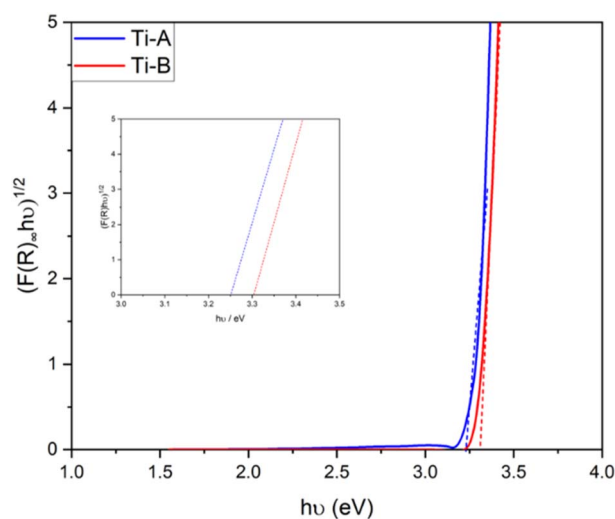

Fig. 3 The bandgap energy value of the prepared samples.

Ti-A exhibited a slightly smaller bandgap compared to Ti-B, which is believed to be due to the light-shielding effect of $TiOF_2$. Consequently, Ti-B possesses a lower absorption capacity than Ti-A.

Scanning electron microscopy (SEM) and transmission electron microscopy (TEM). The sample morphology was assessed through SEM-EDX and TEM analysis, as depicted in Fig. 4 and 5. In theory, both TiO_2 and $TiOF_2$ possess a similar tetragonal and standard cubic structure, characterized by lattice constants of 3.520 Å and 3.798 Å, respectively.[28,29]

Based on the SEM analysis (Fig. 4), the predominant crystal structure observed in the samples is a truncated bipyramid, suggesting the presence of the [001] facet. Ti-B exhibits a flatter structure compared to Ti-A, likely due to its greater growth towards the [001] facet. The elemental composition of Ti, O, and F in both Ti-A and Ti-B was semi-quantitatively analyzed using energy dispersive X-ray spectroscopy (EDX), as summarized in Table 4.
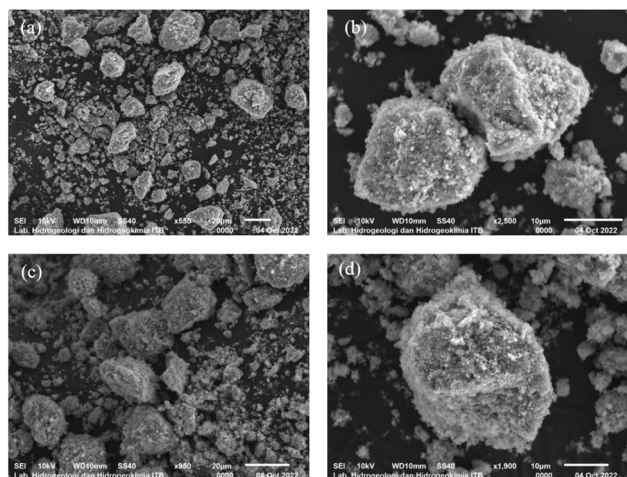
Fig. 4 Structure and morphology samples by SEM (a) and (b) Ti-A and (c) and (d) Ti-B.

Fig. 5 TEM images and electron diffraction pattern of (a–d) Ti-A and (e–h) Ti-B samples.

Table 4 Percentage of the mass element of prepared samples

Mass element (%)	Ti-A	Ti-B
Ti	53.37	45.20
O	36.49	38.97
F	10.14	15.83

Table 5 Physico-chemical surface properties of the prepared samples

Sample	S_{BET} ($m^2\ g^{-1}$)	V_{pore} (cc g^{-1})	D_{pore} (nm)
Ti-A	114.20	0.31	10.94
Ti-B	77.91	0.55	27.96

The quantities of elements in Ti-B, as determined through SEM-EDX analysis (Table 4) confirms the fluorine (F) content surpasses that of Ti-A, which can be attributed to the varying amounts of HF incorporated during the synthesis process.

In addition, TEM analysis (Fig. 5) is used to obtain quantitative measures of size distributions and morphology of Ti-A (Fig. 5a–d) and Ti-B (Fig. 5e–h) samples. As depicted in HR-TEM images (Fig. 5c and g) and corresponding electron diffraction pattern (Fig. 5d and h) for Ti-A and Ti-B samples, the lattice fringes measuring 0.352 nm and 0.38 nm correspond to the (101) planes of TiO_2 (ref. 30) and (100) planes of $TiOF_2$,[16] respectively. This observation aligns with the findings from XRD analyses (Fig. 1). The particle sizes of Ti-A are in the range of 19 to 40 nm with an average size of 27 nm, while Ti-B samples is in the range of 26 to 154 nm with an average size of 72 nm. The even distribution of Ti, O, and F indicates the successful formation of a heterojunction.

N$_2$ adsorption–desorption isotherm. The physicochemical surface characteristics of the photocatalysts were assessed (Table 5) through nitrogen adsorption–desorption analysis. (Fig. 6) displays the adsorption–desorption isotherm profiles for Ti-A and Ti-B. In accordance with the guidelines of the 1985
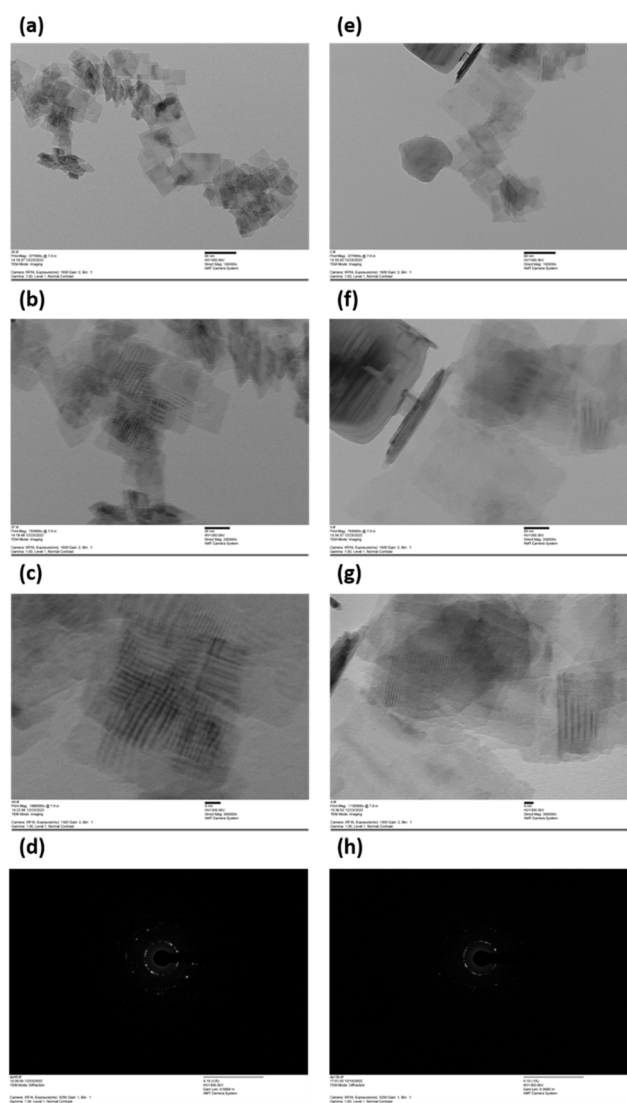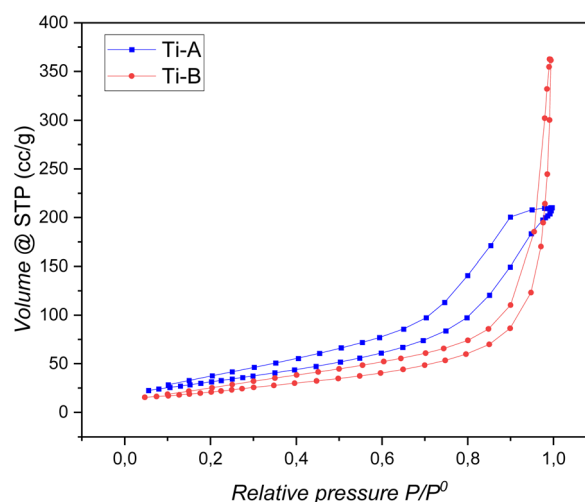

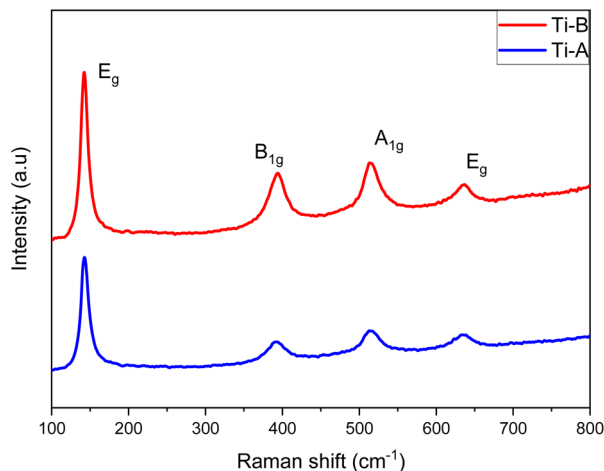Fig. 6 Adsorption–desorption curve of the prepared samples.

Fig. 7 Raman spectra of the samples.

IUPAC physisorption isotherm, both catalysts manifest an isotherm behaviour akin to Type IV(a). Type IV isotherms are typically associated with adsorbents possessing mesoporous structures. The specific surface area of the Ti-A sample exceeded that of Ti-B, measuring 114.20 m^2 g^{-1} and 77.91 m^2 g^{-1}, respectively. A greater specific surface area is advantageous as it offers more active sites during photocatalysis, thereby enhancing the oxidation of methane to methanol on the photocatalyst surface.

The pore volume and size in Ti-B were found to be greater than those in Ti-A, measuring 0.55 cc g^{-1} and 27.60 nm for Ti-B compared to 0.31 cc g^{-1} and 10.94 nm for Ti-A, respectively. In terms of the average pore size, Ti-A and Ti-B both fall within the category of mesoporous catalysts, with average pore sizes of 10.94 nm and 27.96 nm, respectively. Notably, the diameter of both catalysts exceeds that of the reactant (methane) and the product (methanol), which are 3.8 Å and 3.6 Å, respectively. Consequently, it is likely that the adsorption and desorption processes of the reactant and product into the catalyst pores occur without hindrance.

Raman spectroscopy. The local structure of the synthesized samples was additionally validated using Raman spectroscopy, as depicted in Fig. 7. The spectra provided confirmation of the presence of TiO_2, as evidenced by the appearance of four distinct active bands at wavenumbers of 144 (E_g), 396 (B_{1g}), 515 (A_{1g}), and 636 (E_g) cm^{-1} in both samples. The absence of $TiOF_2$ detection is likely attributable to the formation of an *in situ* surface layer of anatase TiO_2, resulting in a minimal amount of enclosed $TiOF_2$, which remained undetectable.[16,17]

Raman spectroscopy provides an alternative means to evaluate the proportion of exposed [001] facets in anatase TiO_2 by capitalizing on distinctive molecular bond vibrations associated with each crystal plane.[28] Specifically, the E_g peak corresponds to the symmetric stretch vibration of O–Ti–O in TiO_2, the B_{1g} peak results from the symmetric bend vibration of O–Ti–O, and the A_{1g} peak is linked to the antisymmetric bend vibration of O–Ti–O. Consequently, as the percentage of exposed [001] facets increase, there is a concurrent rise in the number of symmetric and antisymmetric bend vibrations of O–Ti–O, leading to an augmentation in the intensities of the A_{1g} and B_{1g} peaks observed in the Raman spectrum. Quantitative assessments of the [001] facet percentages can be derived from the ratio of the E_g and A_{1g} peak values within the Raman spectra. The computed percentage values for the [001] facets in both Ti-A and Ti-B are presented in Table 6.

The calculated percentages for Ti-A and Ti-B are 52.4% and 63.8%, respectively. The presence of fluoride (F) ions plays a pivotal role in stabilizing the formation of [001] facets on the surface. Increasing the volume of HF added leads to a higher proportion of exposed [001] facets being formed (Table 6).[20]

Analysis of photocatalytic activity test

Statistical analysis. The yield of methanol production following a 2 hour reaction for each experimental variation are detailed in Table 7.

In run order 5, employing photocatalyst Ti-B along with 15 mL of $FeCl_2$ and 1 mL of H_2O_2, the highest methanol yield was achieved. To comprehensively assess the data pertaining to methanol yield obtained from the specified experimental design, ANOVA analysis was conducted. This analysis aimed to affirm the extent and direction of the factor impacts and identify the variables likely to hold significance, as outlined in Table 8.

The analysis of the experimental data was carried out at a significance level (Type I error) of 0.05. The model exhibited a p-value below the significance level, indicating its significance with a probability of only 0.2% being attributed to noise. Additionally, both main and interaction effects proved to be statistically significant, with p-values below 0.05, as illustrated in Fig. 8.

The catalyst factor exhibited the most pronounced influence on the response, with Ti-A demonstrating a more favorable impact on methanol yield compared to Ti-B. This difference can be attributed to the characteristics of Ti-A, which boasts superior optical properties, a broader surface area, and a larger [001] facet area. The effects of the electron scavenger ($FeCl_2$) and H_2O_2 were also observed to be positive, signifying that an increase in the quantities of $FeCl_2$ and H_2O_2 leads to higher methanol yields. As part of this experimental design, a central point run was conducted to detect any curvature in the response. The p-value associated with curvature, as determined through ANOVA, falls

Table 6 Peak intensity and percentage of [001] facet of samples

Sample	Peak intensity E_g (144 cm^{-1})	Peak intensity A_{1g} (514 cm^{-1})	Percentage [001] (%)
Ti-A	2391.78	1254.47	52.4
Ti-B	3533.55	2256.47	63.8

Table 7 Yield of methanol for each run

Std order	Run order	Catalyst	FeCl$_2$ (mL)	H$_2$O$_2$ (mL)	Yield of methanol (μmol h^{-1} g$_{cat}$$^{-1}$)
5	R1	Ti-A	0.0	1.0	0.6440
1	R2	Ti-A	0.0	0.0	0.5224
6	R3	Ti-B	0.0	1.0	0.2242
10	R4	Ti-B	7.5	0.5	0.4251
7	R5	Ti-A	15.0	1.0	0.7257
4	R6	Ti-B	15.0	0.0	0.3901
3	R7	Ti-A	15.0	0.0	0.4935
2	R8	Ti-B	0.0	0.0	0.3501
8	R9	Ti-B	15.0	1.0	0.3705
9	R10	Ti-A	7.5	0.5	0.6679

Table 8 Analysis of variance (ANOVA) response for methanol yield

Source	DF	Adj SS	Adj MS	F-value	P-value
Model	7	0.229734	0.032819	406.97	0.002
Linear	3	0.179845	0.059948	743.38	0.001
Catalyst	1	0.167272	0.167272	2074.23	0.000
FeCl$_2$	1	0.007144	0.007144	88.59	0.011
H$_2$O$_2$	1	0.005429	0.005429	67.32	0.015
2-Way interactions	3	0.039272	0.013091	162.33	0.006
Catalyst·FeCl$_2$	1	0.002227	0.002227	27.62	0.034
Catalyst·H$_2$O$_2$	1	0.031162	0.031162	386.42	0.003
FeCl$_2$·H$_2$O$_2$	1	0.005883	0.005883	72.95	0.013
Curvature	1	0.010617	0.010617	131.66	0.008
Error	2	0.000161	0.000081		
Total	9	0.229895			

below the significance level, indicating the presence of an optimal response within the tested range of levels.

In this experiment, the absence of replication for each combination posed a potential risk of noise impacting the model's results. To mitigate this concern, we applied the principle of sparsity effect analysis to non-replicated factorial designs. This principle operates under the assumption that the system is primarily influenced by main effects and low-order interactions, enabling us to streamline and derive the most optimal model. Subsequently, through a hierarchical approach, we eliminated higher-order interactions from the Pareto chart, retaining only the most substantial main effects. Fig. 9 visually

represents the absolute values of these effects, organized in descending order of magnitude.

The Pareto chart clearly indicates that all main effects and second-order interactions have a substantial impact on methanol yield. However, it's worth noting that the second-order interactions exhibit comparatively smaller effects when compared to the main effects. In contrast, third-order interactions, particularly those involving the catalyst, FeCl$_2$, and H$_2$O$_2$ factors, do not exert a significant influence on the experimental response. It is important to mention that a 2 full factorial experimental design assumes conditions of constant variance, full randomization, and normally distributed data. To further evaluate the model's adequacy and identify potential variance-related issues, a residual plot analysis was conducted.

Fig. 10 displays the residual plot generated from the experiment. No irregularities or anomalies were observed in any of the residual plots, affirming the validity of the assumptions underlying this experimental design. In standard practice, general regression analysis is commonly employed in 2 full factorial experimental designs to establish an empirical fitting model. However, in this particular experiment, such analysis was not conducted due to the inclusion of qualitative factors. Consequently, interpreting regression results for the factors and response would lack meaningful insight.

Controlled experiments. In order to assess the influence of the photocatalyst and light, several comparative experiments were conducted. These experiments involved using
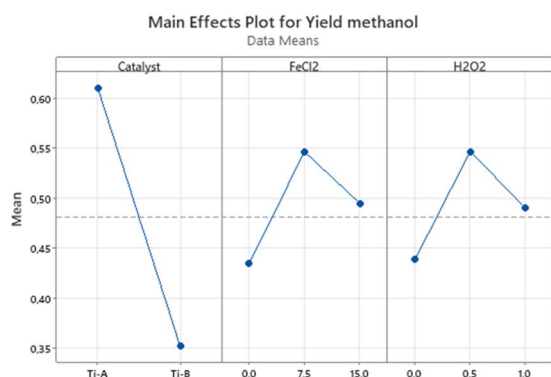
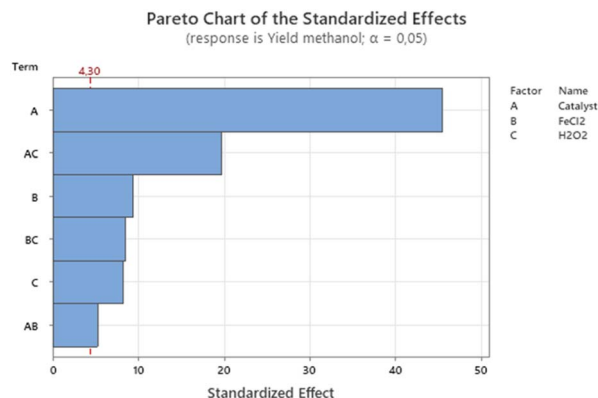**Fig. 8** Main effect plot from the response of methanol yield.

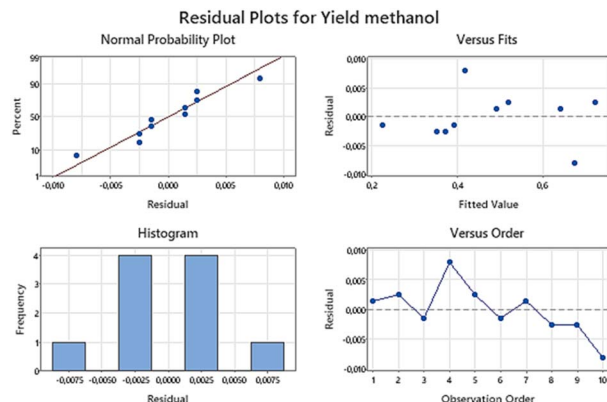**Fig. 9** Pareto chart of the standardized effects.

Fig. 10 Residual plots for yield of methanol.

commercial TiO$_2$, as well as scenarios where no catalyst or no light was applied. The rate of methane consumption (Fig. 11) and the methanol yield (Fig. 12) were monitored at 30 minute intervals throughout a 3 hour reaction period. The $C_t/C_{0,\text{methane}}$ ratio indicates the concentration of methane at a certain time (C_t) compared to the initial concentration of methane gas (C_0) analysed using the Gas Chromatography (GC) instrument.

In the absence of light, methane gas did not exhibit a significant reduction, and no methanol was generated during the reaction. This underscores the role of the TiO$_2$/TiOF$_2$ photocatalyst in facilitating the light-driven conversion of methane into methanol. However, it's worth noting that there was a minor decrease in gas levels over time, possibly because gas was being collected for analysis. When employing the commercial TiO$_2$ catalyst along with the addition of the electron scavenger FeCl$_2$, H$_2$O$_2$, and UV-vis light, there was a reduction in methane levels, but methanol was not detected. This discrepancy could be attributed to methane undergoing reactions to form other compounds besides methanol, which were not identified in this particular study.
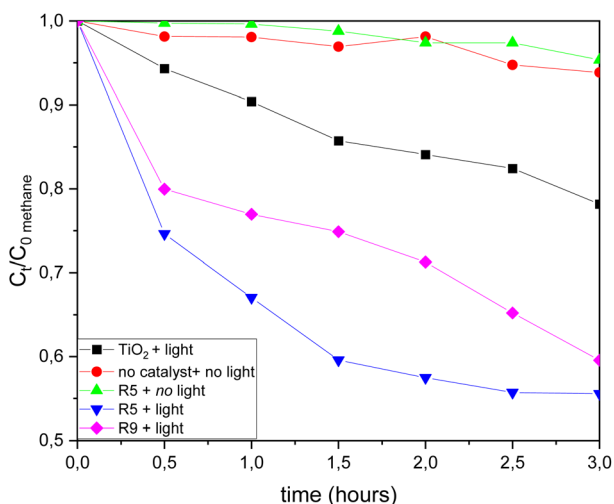
R5 experiment displayed the highest methane consumption (Fig. 11) and methanol production (Fig. 12). Methanol production was observed between 0.5 and 2.5 hours of the reaction, with a decline in methanol production occurring after the 2.5 hour mark. This decrement could be attributed to the degradation of methanol into other products, especially at certain concentrations, as methanol is susceptible to be oxidized. An excess of $^\bullet$O$_2$ and a certain level of methanol can result in further oxidation into various compounds. Additionally, it is worth noting that the [001] facet of the catalyst possesses oxidative properties. A greater presence of [001] facets renders the catalyst more oxidative,[31] leading to increased charge carriers and enhanced separation efficiency of photogenerated electron–hole pairs.[17] Consequently, in R9, which employs Ti-B with a higher proportion of [001] facets compared to Ti-A, the production and subsequent decline of methanol appear to occur more rapidly.

The inclusion of fluorine (F) in the TiO$_2$/TiOF$_2$ composite serves several beneficial purposes: it enhances the adsorption of reactant molecules on the catalyst surface,[26] reduces the crystal surface energy to foster the formation of [001] facets, and diminishes light scattering by replacing high-scattering oxygen atoms with low-scattering fluorine atoms.[5] This, in turn, helps prevent recombination and prolongs the lifetimes of charge carriers.[17,32] The presence of both FeCl$_2$ and H$_2$O$_2$ has been demonstrated to have a positive impact on the reaction. The results obtained from ANOVA indicate that the main effects and second-order interaction effects of these compounds with the catalyst contribute significantly to efficient methanol production. This can be elucidated by the role played by Fe^{2+} ions and H$_2$O$_2$ in facilitating the Fenton reaction cycle. Fenton reactions are instrumental in generating free radicals and reducing the recombination of electron–hole pairs, primarily through the production of Fe^{3+} within the Fenton cycle.[33] Furthermore, the assessment of photocatalytic activity depicted in Fig. S1† highlights that incorporating metallic Ag in Ag-TiO$_2$/TiOF$_2$ significantly enhances methane-to-methanol conversion, with a 2.2-fold increase in activity compared to TiO$_2$/
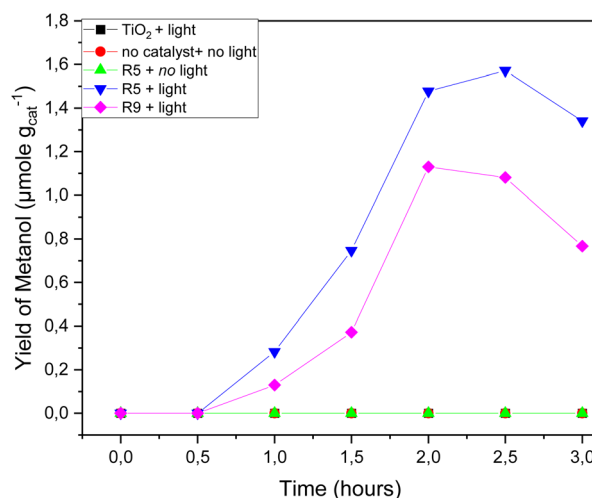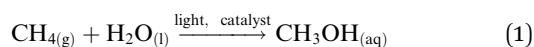

Fig. 11 Methane consumption in the comparative experiments.

Fig. 12 Yield of methanol in the comparative experiments.

$TiOF_2$. The observed methanol yield of 1.5817 μmole h^{-1} g_{cat}^{-1} underscores the catalytic efficacy of Ag, suggesting that the presence of metallic Ag contributes positively to the photocatalytic performance of the system.

Kinetic study. To evaluate the photocatalytic activity in the conversion of methane to methanol, the kinetics investigation for achieving the highest methanol yield was conducted. Under the assumption that the reaction is governed by surface chemical processes occurring on the catalyst, we can simplify and represent the photocatalytic conversion of methane to methanol as shown in eqn (1).

$$CH_{4(g)} + H_2O_{(l)} \xrightarrow{\text{light, catalyst}} CH_3OH_{(aq)} \qquad (1)$$

The photocatalytic reaction took place within a batch reactor, where methane gas (CH_4) was introduced into water (H_2O) for a specific duration until saturation was reached. Given the low solubility of methane in water, each dissolved methane molecule swiftly engaged in a reaction with water during the process. As a result, there was an excess of water acting as the reactant in this reaction. Consequently, the kinetics of the photocatalytic conversion of methane to methanol can be accurately modelled using pseudo-first-order reaction kinetics following eqn (2).

$$\ln \frac{C_{0,\text{methane}}}{C_{t,\text{methane}}} = kt \qquad (2)$$

Table 9 displays the reaction rate constants for both catalysts, Ti-A and Ti-B, when subjected to the same quantities of added $FeCl_2$ and H_2O_2. Notably, the rate constant for catalyst Ti-A is higher in comparison to Ti-B. This observation is consistent with the ANOVA findings, which suggest that Ti-A has a more substantial impact than Ti-B, resulting in a faster reaction rate. Table 10 provides the contrast of methanol yield observed in this research compare to that of another study involving a pure titanium-based photocatalyst.

Table 9 The rate constant for the photocatalytic reaction of methane to methanol

Run order	Catalyst	k (minute^{-1})	R^2
5	Ti-A	0.1080	0.93
9	Ti-B	0.0784	0.96

Proposed mechanism. Titanium dioxide (TiO_2) is known to exhibit a drawback of high visible light scattering. $TiOF_2$ is proposed as a heterojunction with TiO_2 photocatalyst due to it has lower visible light scattering and superior visible light absorption capabilities compared to TiO_2.[5] The conduction band (CB) and valence band (VB) edge potentials of TiO_2 and $TiOF_2$ can be determined using specific equation involving absolute electronegativity, bandgap energy and energy of free electron. Previous report[17] provides and calculates the CB potential of TiO_2 and $TiOF_2$ as -0.34 eV and 1.18 eV, respectively. The corresponding VB potential for TiO_2 and $TiOF_2$ are 2.5 eV and 4.38 eV, respectively.

The mechanism reaction proposed from the photocatalytic reaction of methane to methanol in the system with presence of $TiO_2/TiOF_2$, $FeCl_2$ and H_2O_2 can be illustrated in Fig. 13.

Upon the illumination of light, electron (e^-) from TiO_2 and $TiOF_2$ exited to the higher energy level, leaving a vacant valence band with holes (h^+). Photogenerated electrons and protons migrate in the interface between two semiconductors. The CB and the VB levels of TiO_2 are higher than the corresponding levels of the $TiOF_2$. Thus, the photogenerated electrons will transfer to $TiOF_2$, while the photogenerated holes will migrate to TiO_2.

Reduction reaction and the oxidation reaction take place on $TiOF_2$ with lower reduction potential and on TiO_2 with lower oxidation potential, respectively.[36] The electrons in the conduction band reacts with Fe^{3+} to form Fe^{2+} and subsequently reacts with H_2O_2 to form Fe^{3+} and $^{\bullet}OH$. The protons in the valence band oxidize CH_4 and H_2O to form radical $^{\bullet}CH_3$ and $^{\bullet}OH$, respectively. The $^{\bullet}CH_3$ radical reacts with $^{\bullet}OH$ to produces CH_3OH. Based on Fig. S2,† an increase of the $^{\bullet}OH$ presence was observed by increasing photocatalytic reaction time using $TiO_2/TiOF_2$ and Ag-$TiO_2/TiOF_2$ compared to without the presence of catalyst. The comparative analysis of photocatalytic methane-to-methanol conversion, both in the presence and absence of coumarin as a hydroxyl radical scavenger, reveals a substantial decrease in methanol yield, as depicted in Fig. S3.† The observed significant reduction, or even negligible production, of methanol in the presence of scavengers strongly suggests the crucial involvement of hydroxyl radicals in the intricate reaction mechanism governing the conversion of methane to methanol. Alternatively, the $^{\bullet}OCH_3$ radical, generated from the reaction between CH_4 and $^{\bullet}O_2^-$, reacts with H_2O to produce the product CH_3OH. In summary, the mechanism of photocatalytic conversion of

Table 10 Comparison of yield methanol among TiO_2 based photocatalyst

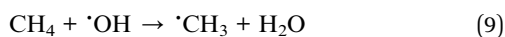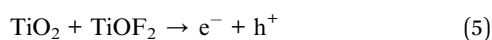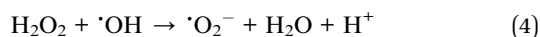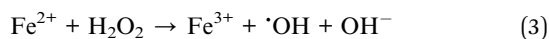| Catalyst	Reaction condition	Light source	Yield of methanol	Ref.
Ag-$TiO_2/TiOF_2$	1 atm, room temperature, $FeCl_2$, H_2O_2	Xenon lamp (UV-vis light 300 W)	1.58 μmole h^{-1} g_{cat}^{-1}	This study
$TiO_2/TiOF_2$	1 atm, room temperature, $FeCl_2$, H_2O_2	Xenon lamp (UV-vis light 300 W)	0.73 μmole h^{-1} g_{cat}^{-1}	This study
Pure TiO_2	1 atm, room temperature	Nd:YAG laser (355 nm)	~86 μmole h^{-1}	34
m-TiO_2	1 atm, 55–60 °C	UV light (400 W)	0.02 μmole h^{-1}	7
TiO_2/Bi_2WO_6	55 °C, medium pressure	Mercury lamp (450 W)	~10 μmole h^{-1} g^{-1}	35
Cu_2O/TiO_2	1 atm, room temperature, H_2O_2	Xenon lamp (UV-vis light 300 W)	~3 μmole h^{-1} g_{cat}^{-1}	6
FeO_x/TiO_2	1 atm, room temperature, H_2O_2	Xenon lamp (UV-vis light 300 W)	360 μmole h^{-1} g_{cat}^{-1}	6

Fig. 13 The proposed reaction scheme of methanol production on the TiO$_2$/TiOF$_2$ photocatalyst.

methane to methanol involve FeCl$_2$ and H$_2$O$_2$ was speculated as follow eqn (3–12):

$$Fe^{2+} + H_2O_2 \rightarrow Fe^{3+} + {}^\cdot OH + OH^- \tag{3}$$

$$H_2O_2 + {}^\cdot OH \rightarrow {}^\cdot O_2^- + H_2O + H^+ \tag{4}$$

$$TiO_2 + TiOF_2 \rightarrow e^- + h^+ \tag{5}$$

$$Fe^{3+} + e^- \rightarrow Fe^{2+} \tag{6}$$

$$H_2O_2 + e^- \rightarrow {}^\cdot OH \tag{7}$$

$$CH_4 + h^+ \rightarrow {}^\cdot CH_3 \tag{8}$$

$$CH_4 + {}^\cdot OH \rightarrow {}^\cdot CH_3 + H_2O \tag{9}$$

$$CH_4 + {}^\cdot O_2^- \rightarrow {}^\cdot OCH_3 + OH^- \tag{10}$$

$${}^\cdot CH_3 + {}^\cdot OH \rightarrow CH_3OH \tag{11}$$

$${}^\cdot OCH_3 + H_2O \rightarrow CH_3OH + {}^\cdot OH \tag{12}$$
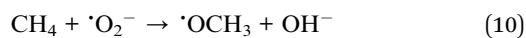
Conclusions

In summary, we have successfully developed a heterojunction TiO$_2$/TiOF$_2$ photocatalyst through a one-step hydrothermal method. This modified photocatalyst exhibited truncated bipyramidal shapes, indicating the presence of exposed [001] facets. Our statistical analysis confirmed the significant influence of this modified photocatalyst on methanol production. Moreover, the combined use of photocatalyst TiO$_2$/TiOF$_2$ with the electron scavenger FeCl$_2$ and H$_2$O$_2$ demonstrated a positive synergistic effect on methane-to-methanol conversion, yielding 0.7257 µmole (g$_{cat}$ h)$^{-1}$ of methanol. Introducing Ag onto the TiO$_2$/TiOF$_2$ catalyst demonstrates a notable 2.2-fold improvement in the methanol yield. Moreover, the pivotal role of hydroxyl radicals in the overall reaction mechanism underscores their significance in influencing the photocatalytic conversion of methane to methanol process. Ultimately, this report paves the way for optimizing methanol yield by pinpointing the crucial factors involving TiO$_2$/TiOF$_2$ photocatalyst, FeCl$_2$, H$_2$O$_2$, and Ag metal, thus leading to the best possible response.

Author contributions

Conceptualization, WHS and DS; methodology, GY, WHS, and DS; formal analysis, GY and WHS; investigation, GY and WHS; resources, WHS and DS; writing – original draft preparation, WHS and GY; writing – review and editing, WHS and DS; visualization, GY; supervision, WHS and DS; project administration, WHS; funding acquisition, WHS and DS. All authors have read and agreed to the published version of the manuscript.

Conflicts of interest

There is no conflict of interests existing in the manuscript submission, and it is approved by all of the authors for publication. All the authors listed have approved the manuscript to be enclosed.

Acknowledgements

Notes and references

1 X. Meng, X. Cui, N. P. Rajan, L. Yu, D. Deng and X. Bao, Direct Methane Conversion under Mild Condition by Thermo-, Electro-, or Photocatalysis, *Chem*, 2019, **5**(9), 2296–2325, DOI: **10.1016/j.chempr.2019.05.008**.

2 D. Yu, Y. Jia, Z. Yang, et al., Solar Photocatalytic Oxidation of Methane to Methanol with Water over RuOx/ZnO/CeO2Nanorods, *ACS Sustain. Chem. Eng.*, 2022, **10**(1), 16–22, DOI: **10.1021/acssuschemeng.1c07162**.

3 V. Augugliaro, G. Palmisano, L. Palmisano and J. Soria, *Heterogeneous Photocatalysis and Catalysis: an Overview of Their Distinctive Features*, Elsevier B.V., 2019, DOI: **10.1016/B978-0-444-64015-4.00001-8**.

4 Z. Xiong, H. Wu, L. Zhang, Y. Gu and X. S. Zhao, Synthesis of TiO2 with controllable ratio of anatase to rutile, *J. Mater. Chem. A*, 2014, **2**(24), 9291–9297, DOI: **10.1039/c4ta01144a**.

5 X. Rocquefelte, F. Goubin, Y. Montardi, et al., Analysis of the refractive indices of TiO 2, TiOF 2, and TiF 4: Concept of optical channel as a guide to understand and design optical materials, *Inorg. Chem.*, 2005, **44**(10), 3589–3593, DOI: **10.1021/ic048259w**.

6 J. Xie, R. Jin, A. Li, et al., Highly selective oxidation of methane to methanol at ambient conditions by titanium dioxide-supported iron species, *Nat. Catal.*, 2018, **1**(11), 889–896, DOI: **10.1038/s41929-018-0170-x**.

7 Y. Negishi, S. Watanabe, M. Aoki, S. Hossain and W. Kurashige, Toward the Creation of Highly Active Photocatalysts That Convert Methane into Methanol Active Photocatalysts, *Antimicrob. Agents Chemother.*, 2019, **32**(12), 1854–1858, DOI: **10.1128/AAC.32.12.1854**.

8 J. Zhu, Z. Liu, F. Yang, D. Long, Y. Jian and S. Pu, The Preparation of {001}TiO2/TiOF2 via a One-Step Hydrothermal Method and Its Degradation Mechanism of Ammonia Nitrogen, *Materials*, 2022, **15**(18), 6465, DOI: **10.3390/ma15186465**.

9 J. Li, X. Lv, B. Weng, M. B. J. Roeffaers and H. Jia, Engineering light propagation for synergetic photo- and thermocatalysis toward volatile organic compounds elimination, *Chem. Eng. J.*, 2023, **461**, 142022, DOI: **10.1016/j.cej.2023.142022**.

10 G. Yuniar, W. H. Saputera, D. Sasongko, R. R. Mukti, J. Rizkiana and H. Devianto, Recent Advances in Photocatalytic Oxidation of Methane to Methanol, *Molecules*, 2022, **27**, 5496, DOI: **10.3390/molecules27175496**.

11 D. Yu, H. Zhang, H. Liu, *et al.*, Strategies for Improving the Photocatalytic Methane to Methanol Conversion Efficiency, *Curr. Org. Chem.*, 2023, **27**, 399–410, DOI: **10.2174/1385272827666221219112052**.

12 C. Wang, H. Zhang, F. Lai, *et al.*, Engineering versatile Au-based catalysts for solar-to-fuel conversion, *J. Energy Chem.*, 2023, **83**, 341–362, DOI: **10.1016/j.jechem.2023.04.027**.

13 N. Syuhada, W. Loon and D. Mohamad, ScienceDirect A critical review of metal-doped TiO 2 and its structure e physical properties e photocatalytic activity relationship in hydrogen production, *Int. J. Hydrogen Energy*, 2020, **45**(53), 28553–28565, DOI: **10.1016/j.ijhydene.2020.07.233**.

14 S. P. Hong, S. Kim, N. Kim, J. Yoon and C. Kim, Invited Review Paper A short review on electrochemically self-doped TiO2 nanotube arrays: Synthesis and applications, *Korean J. Chem. Eng.*, 2019, **36**(11), 1753–1766, DOI: **10.1007/s11814-019-0365-0**.

15 S. Murcia-López, K. Villa, T. Andreu and J. R. Morante, Improved selectivity for partial oxidation of methane to methanol in the presence of nitrite ions and BiVO4 photocatalyst, *Chem. Commun.*, 2015, **51**(33), 7249–7252, DOI: **10.1039/c5cc00978b**.

16 C. Z. Wen, Q. H. Hu, Y. N. Guo, X. Q. Gong, S. Z. Qiao and H. G. Yang, From titanium oxydifluoride (TiOF2) to titania (TiO2): Phase transition and non-metal doping with enhanced photocatalytic hydrogen (H2) evolution properties, *Chem. Commun.*, 2011, **47**(21), 6138–6140, DOI: **10.1039/c1cc10851d**.

17 R. Liu, Z. Ji, S. Xie, *et al.*, Fabrication of {001}-facet enriched anatase TiO2/TiOF2 heterostructures with controllable morphology for enhanced photocatalytic activity, *Mater. Today Commun.*, 2021, **26**, 102060, DOI: **10.1016/j.mtcomm.2021.102060**.

18 Z. Liu, X. Liu, Q. Lu, Q. Wang and Z. Ma, TiOF2/TiO2 composite nanosheets: Effect of hydrothermal synthesis temperature on physicochemical properties and photocatalytic activity, *J. Taiwan Inst. Chem. Eng.*, 2019, **96**, 214–222, DOI: **10.1016/j.jtice.2018.11.013**.

19 Y. Zhang, T. Xia, M. Shang, *et al.*, Structural evolution from TiO2 nanoparticles to nanosheets and their photocatalytic performance in hydrogen generation and environmental pollution removal, *RSC Adv.*, 2014, **4**(31), 16146–16152, DOI: **10.1039/c3ra48066f**.

20 X. Han, Q. Kuang, M. Jin, Z. Xie and L. Zheng, Synthesis of Titania Nanosheets with a High Percentage of Exposed (001) Facets, *J. Am. Chem. Soc.*, 2009, **131**(001), 3152–3153.

21 K. Thamaphat, P. Limsuwan and B. Ngotawornchai, Phase Characterization of TiO$_2$ Powder by XRD and TEM, *Nat. Sci.*, 2008, **42**(5), 357–361.

22 J. Wang, F. Cao, Z. Bian, K. H. Leung and H. Li, Ultrafine single-crystal TiOF2 nanocubes with mesoporous structure, high activity and durability in visible light driven photocatalysis, *Nanoscale*, 2014, **6**, 897–902, DOI: **10.1039/c3nr04489k**.

23 W.-J. Ong, L.-L. Tan, S.-P. Chai, S. T. Yonga and A. R. Mohamed, Highly Reactive {001} Facets of TiO2-Based Composites: Synthesis, View Article Online DOI: 10.1039/C3NR04655A Formation Mechanism and Characterizations, *Nanoscale*, 2014, **6**(207890), 1946–2008, DOI: **10.1039/C3NR04655A**.

24 W. Ong, L. Tan, S. Chai and S. Yong, Facet-Dependent Photocatalytic Properties of TiO$_2$-Based Composites for Energy Conversion and Environmental Remediation, *ChemSusChem*, 2014, **7**(3), 690–719, DOI: **10.1002/cssc.201300924**.

25 C. Hou, H. Liu and Y. Li, The preparation of three-dimensional flower-like TiO$_2$/TiOF$_2$ photocatalyst and its efficient degradation of tetracycline hydrochloride, *RSC Adv.*, 2021, **11**(25), 14957–14969, DOI: **10.1039/d1ra01772a**.

26 J. Hu, Y. Lu, X. L. Liu, *et al.*, Photoinduced terminal fluorine and Ti3+ in TiOF2/TiO2 heterostructure for enhanced charge transfer, *CCS Chem.*, 2020, **2**(6), 1573–1581, DOI: **10.31635/ccschem.020.202000305**.

27 W. H. Saputera, J. Rizkiana and W. Wulandari, Role of defects on TiO2/SiO2 composites for boosting photocatalytic water splitting Wibawa, *RSC Adv.*, 2020, **10**, 27713–27719, DOI: **10.1039/d0ra05745b**.

28 F. Tian, Y. Zhang, J. Zhang and C. Pan, Raman spectroscopy: A new approach to measure the percentage of anatase TiO2 exposed (001) facets, *J. Phys. Chem. C*, 2012, **116**(13), 7515–7519, DOI: **10.1021/jp301256h**.

29 Z. Wang, B. Huang, Y. Dai, *et al.*, Topotactic transformation of single-crystalline TiOF 2 nanocubes to ordered arranged 3D hierarchical TiO 2 nanoboxes, *CrystEngComm*, 2012, **14**(14), 4578–4581, DOI: **10.1039/c2ce25271f**.

30 L. Niu, Q. Zhang, J. Liu, J. Qian and X. Zhou, TiO 2 nanoparticles embedded in hollow cube with highly exposed { 001 } facets : Facile synthesis and photovoltaic applications, *J. Alloys Compd.*, 2016, **656**, 863–870, DOI: **10.1016/j.jallcom.2015.10.039**.

31 L. Ye, J. Mao, J. Liu, Z. Jiang, T. Peng and L. Zan, Synthesis of anatase TiO2 nanocrystals with {101}, {001} or {010} single facets of 90% level exposure and liquid-phase photocatalytic reduction and oxidation activity orders, *J.*

Mater. Chem. A, 2013, **1**(35), 10532–10537, DOI: **10.1039/c3ta11791j**.

32 X. Zhao, G. Wei, J. Liu, Z. Wang, C. An and J. Zhang, Synthesis of heterostructured Pd@TiO2/TiOF2 nanohybrids with enhanced photocatalytic performance, *Mater. Res. Bull.*, 2016, **80**, 337–343, DOI: **10.1016/j.materresbull.2016.04.018**.

33 Y. Zeng, H. C. Liu, J. S. Wang, X. Y. Wu and S. L. Wang, Synergistic photocatalysis-Fenton reaction for selective conversion of methane to methanol at room temperature, *Catal. Sci. Technol.*, 2020, **10**(8), 2329–2332, DOI: **10.1039/d0cy00028k**.

34 M. A. Gondal, A. Hameed, Z. H. Yamani and A. Arfaj, Photocatalytic transformation of methane into methanol under UV laser irradiation over WO3, TiO2 and NiO catalysts, *Chem. Phys. Lett.*, 2004, **392**(4–6), 372–377, DOI: **10.1016/j.cplett.2004.05.092**.

35 S. Murcia-López, K. Villa, T. Andreu and J. R. Morante, Partial oxidation of methane to methanol using bismuth-based photocatalysts, *ACS Catal.*, 2014, **4**(9), 3013–3019, DOI: **10.1021/cs500821r**.

36 J. Low, J. Yu, M. Jaroniec, S. Wageh and A. A. Al-Ghamdi, Heterojunction Photocatalysts, *Adv. Mater.*, 2017, **29**(20), 1–20, DOI: **10.1002/adma.201601694**.